Stratification and turbulence in subtidal channels through intertidal mudflats

David K. Ralston and Mark T. Stacey

Department of Civil and Environmental Engineering, University of California, Berkeley, California, USA

[1]   Field observations in San Francisco Bay of subtidal channels that drain through intertidal mudflats indicate that substantial periodic stratification develops in very shallow flows with distinct asymmetries between flood and ebb conditions. The greatest variability in salinity and stratification occurs during the wet winter months. Very strong longitudinal salinity gradients develop across the intertidal zone, between salty subtidal water and fresher water draining into the marsh upstream. Tidal straining of the longitudinal gradient creates the periodic stratification, stratifying through ebbs and destratifying through floods. The stratification can be very strong in very shallow flows, with $N^2 > 0.1$ s^{-2} in about 0.5 m water depth. Analysis of the data with dimensionless numbers shows that at times the stratification is strong enough to suppress turbulence and mixing. The asymmetry in stratification between ebbs and floods results in asymmetries in eddy viscosity and eddy diffusivity, with lower values during the stratified ebbs. Because of the intertidal elevation of the system, the strong longitudinal salinity gradient is regenerated each time the mudflats and marsh drain. The system approaches a tidally periodic steady state where the flow dynamics are dominated by the sharp front of salty water that advects into the intertidal zone on the rising tide and exits the system by each lower low water. The field data are supported by a numerical model with simple mudflat/channel bathymetry. Both the field and numerical work indicate that the shallow, low energy flows in mudflat channels transition between strongly stratified suppressed turbulence and relatively unstratified active turbulence each tidal cycle.

1. Introduction

[2]   Intertidal mudflats and salt marshes at the margins of many estuaries provide important habitat for diverse aquatic and terrestrial organisms. Flow and scalar transport govern the morphology and functional characteristics of these systems by distributing salt, sediments, organisms, and potentially contaminants. While there has been extensive study of the biology of these very shallow (and periodically dry) locations [e.g., *Blanchard et al.*, 2001; *Widdows and Brinsley*, 2002], little work has focused on the flow dynamics in these environments. We report here on highly variable dynamics in a subtidal mudflat channel, particularly the importance of very strong periodic stratification and longitudinal density gradients. Salinity stratification becomes strong enough at times during the tidal cycle to suppress turbulent motions and limit turbulent mixing of scalars. Vertical distributions of sediment and biological scalars are controlled in part by stratification and mixing. Unsteadiness or asymmetry in vertical mixing through the tidal cycle affects the net transport of scalars into or out of the intertidal zone.

1.1. Intertidal Setting

[3]   Sediment transport has received substantial attention in intertidal zone research because it is critical to the morphology of these environments. Studies have considered hydrodynamics and sediment properties on mudflats [*Dyer et al.*, 2000; *Christie et al.*, 1999] and in salt marshes [*Christiansen et al.*, 2000]. Studies have documented how intertidal transport depends on tidal currents, wind waves [*Dyer et al.*, 2000], episodic storm events [*Leonard et al.*, 1995], and vegetation [*Christiansen et al.*, 2000]. Although some note salinity variability at the study sites, salinity stratification is rarely discussed as a major factor for the hydrodynamics and sediment transport.

[4]   Salinity dynamics have not been considered on mudflats in part because of the limited spatial and temporal scales of field investigations. Most research has concentrated on the vast expanse of intertidal mudflats rather than the subtidal channels that pass through the mudflats [*Shi and Chen*, 1996]. Tidal channels are small in surface area relative to the mudflats, but they continue to drain water out to the subtidal zone after the receding tide has exposed mudflat and marsh surfaces. As a result, the time-integrated transport in channels can be substantial [*Christiansen et al.*, 2000]. Much of the research on tidal channels has been morphological to document how tidal forcing influences their size and location

[*Wells et al.*, 1990; *Leopold et al.*, 1993; *Friedrichs*, 1995; *Fagherazzi and Furbish*, 2001]. Morphological studies tend to consider very long timescales, averaging over tidal timescale variability that will be our focus. There have been few detailed studies of the hydrodynamics in subtidal channels. The observations we present here indicate that in many ways the dynamics of these shallow, low energy flows are analogous to estuarine flows of much larger spatial scales. Flow in subtidal channels can transition from strongly stratified to partially mixed to nearly well-mixed each tidal cycle.

1.2. Stratification and Turbulence in Shallow Tidal Systems

[5] In estuarine flows, stratification is important because it inhibits turbulence, affecting residual velocities, scalar mixing, and net transport. The degree of stratification depends on freshwater flow, tidal currents, and longitudinal density gradients. Consequently, timescales of variability for stratification can range from seasonal (variations in river flow) to fortnightly (spring-neap modulation in mixing energy [*Peters*, 1997]) to tidal (ebb/flood asymmetries [*Nepf and Geyer*, 1996; *Stacey et al.*, 1999]). On the tidal timescale, straining of the density gradient through ebbs enhances stratification, while the opposite sign of velocity shear during floods tends to homogenize the water column and reduce stratification [*Simpson et al.*, 1990]. This strain-induced periodic stratification (SIPS) creates asymmetry in stratification between ebb and flood. Tidal straining is an important process in larger estuaries [*Nepf and Geyer*, 1996] and coastal settings [*Rippeth et al.*, 2001], but few have considered it in very shallow environments. *Chant and Stoner* [2001] found that in a shallow estuary (~2 m deep) tidal straining in combination with flood dominance generated periodic stratification and net sediment transport up estuary. *Stevens* [2003] observed in an enclosed estuarine embayment that low tidal energy permitted substantial stratification and suppressed turbulent mixing even with very little freshwater flow.

[6] Generally, stratified turbulence has been studied in estuaries that are much larger and deeper than the intertidal region we will consider here. The balance between turbulence and stratification in the intertidal zone will be the focus of this work. In particular, we examine how turbulence evolves through the tidal cycle using length scales that characterize both turbulent motions and how strongly stratification suppresses those motions. Investigators have used this approach to measure the effects of stratification on flow dynamics in other estuarine cases [*Ivey and Imberger*, 1991; *Stacey et al.*, 1999]. We measure local velocity fluctuations, velocity shear, and salinity stratification in a subtidal channel to calculate three length scales. The Ozmidov scale represents the scale of largest overturns in stratified flow: $l_O = (\varepsilon/N^3)^{1/2}$, where ε is the dissipation and N is the buoyancy frequency. An Ellison scale with velocity fluctuations rather than density represents the dominant scale of turbulent motions: $l_E = [\overline{u'u'}/(\partial U/\partial z)^2]^{1/2}$ where $\overline{u'u'}$ is the along-channel component of turbulent kinetic energy and $\partial U/\partial z$ is the along-channel shear [*Itsweire et al.*, 1993]. Finally, the Kolmogorov scale represents the scale of the smallest turbulent eddies: $l_K = (\nu^3/\varepsilon)^{1/4}$, where ν is the kinematic viscosity.

[7] Ratios of these three length scales can characterize the turbulence state in a flow [*Ivey and Imberger*, 1991]. The largest turbulent scale (l_O) and active turbulent scale (l_E) yield a turbulent Froude number: $Fr_t = (l_O/l_E)^{2/3}$. For $Fr_T > 1$, turbulence proceeds largely unaffected by stratification, while for $Fr < 1$, turbulent motions are inhibited by stratification. The ratio of the active scale (l_E) and the smallest turbulent scale (l_K) is the turbulent Reynolds number: $Re_t = (l_E/l_K)^{4/3}$. The final combination uses the largest (l_O) and smallest scales (l_K) in a small-scale Froude number: $Fr_\gamma = (l_O/l_K)^{2/3}$. Fr_γ is analogous to an activity parameter for the transition between turbulent motions and internal waves: $[\varepsilon/(\nu N^2)]^{1/2}$ [*Gibson*, 1986]. Observations of these dimensionless numbers in the Hudson River estuary have seen limited application to estuarine environments. Observations in the Hudson River estuary [*Peters*, 1997] and San Francisco Bay [*Stacey et al.*, 1999] indicated that turbulence varied from active to weak, but rarely was completely extinguished by stratification. We will apply this analysis to see how stratification and turbulence in intertidal zone vary on the tidal timescale, and consequences for mixing of momentum and scalars. Longitudinal dispersion, lateral exchange between channels and shoals, and sediment transport all depend on intertidal turbulence and stratification, but these topics will be pursued in other manuscripts [*Ralston and Stacey*, 2005] (also D. K. Ralston, Sediment transport in the intertidal zone over tidal and seasonal timescales, manuscript in preparation, 2005).

2. Field Experiment

[8] The field observations were made at the eastern edge of Central San Francisco Bay at the University of California's Richmond Field Station (Figures 1a and 1b). The Field Station has an intertidal zone with mudflats and salt marsh bisected by two subtidal channels. The channels drain small watersheds upstream of the field site. Urban and industrial areas surround the property, and development has left behind structures that now impact site geometry. Two breakwaters protect the southern edge of the salt marsh, reducing its exposure to wave energy and allowing infilling of sediment and vegetation. Similarly, the berm from abandoned railroad tracks borders the northern edge of the mudflat and salt marsh has filled in behind it. Although the local bathymetry has been modified by these structures, the mudflats and marsh remain representative of similar intertidal regions around San Francisco Bay.

[9] The goal of this set of experiments was to study spatial variability in flow dynamics across the mudflat. Data collection was designed to characterize gradients between subtidal channels and intertidal shoals, and between higher elevation mudflats near the marsh and lower elevation mudflats near the bay. Two sawhorse frames with near-bed instruments were placed at three locations: on the intertidal mudflats (Figure 1a, shoal), in the subtidal channel near the bay (outer channel), and in the subtidal channel near the marsh (inner channel). The frames were oriented along the primary flow axis at each location. The frames had acoustic Doppler velocimeters (ADVs), conductivity-temperature-depth sensors (CTDs), and optical backscatter sensors (OBSs) at fixed elevations within about 0.5 m of the
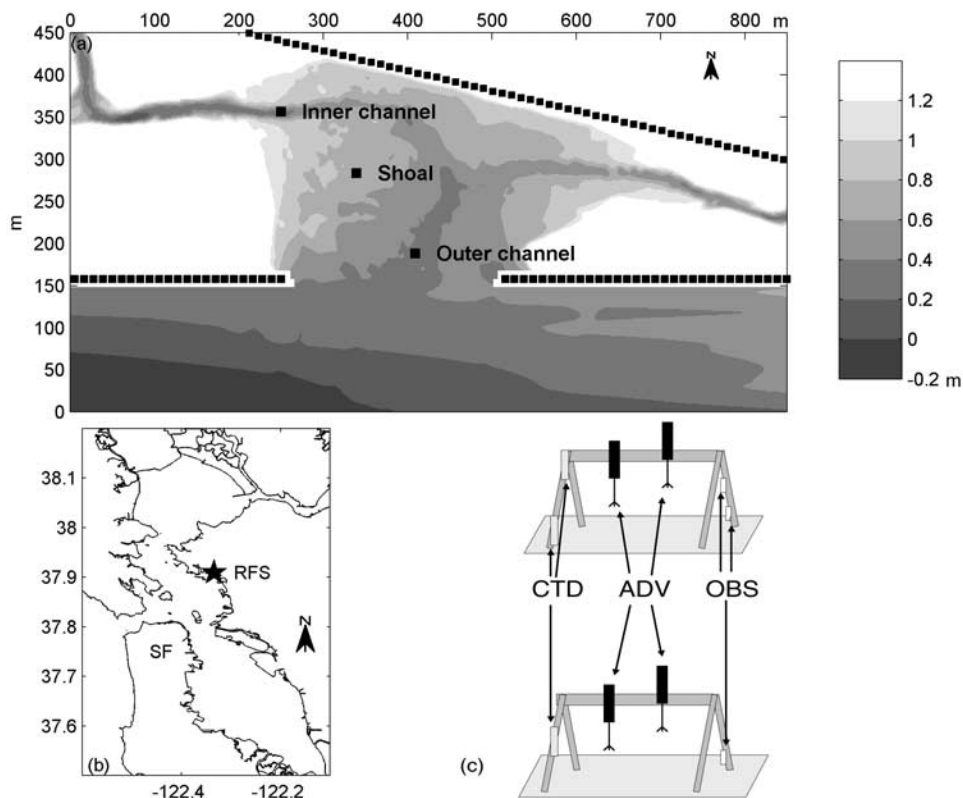
Figure 1. (a) Bathymetry of the study area; mudflats are shaded and vegetated salt marsh is white. Instrument locations for the three study locations are marked on the mudflats. The breakwaters that bound the southern edge of the marsh and the railroad berm that crosses the northern edge of the site are also marked. (b) Location of the field site (RFS) in Central San Francisco Bay. (c) The configurations of the instrument frames. The frames were deployed along the primary flow axis at each study location separated by about 100 m.

bed (Figure 1c). On both frames the ADVs were positioned at 10 cm and 35 cm above the bed and sampled at 8 Hz; burst sampling was every 20 min, with the lower ADV recording for 19.5 min and the upper ADV recording for 10 min. The CTDs on one frame (A) were positioned 10 cm and 65 cm above the bed, and a single CTD on the other frame (B) was 35 cm above the bed. The lower CTD on Frame A sampled every 30 s, while the other two CTDs sampled at the beginning of each ADV burst (every 20 min). The instruments were deployed at each location for about 25 hours (one diurnal tidal cycle) before they were moved to the next location. At the inner channel location the two frames were positioned adjacent to each other for an additional 2 days of data collection at the end of the experiment.

[10] San Francisco Bay has in a Mediterranean climate, so the dominant seasonal variability is between the wet winters and dry summers. To study the mudflats during both freshwater forcing periods, we deployed instruments during dry season (2 to 5 November 2002) and wet season (25 February to 2 March 2003) conditions. Because of the short duration the experiments, tidal forcing did not change significantly over the 3-day deployments. Tides in San Francisco Bay are mixed semi-diurnal, and both experiments were during neap periods when diurnal asymmetry is greater than during springs. There was no precipitation

during either study period, but conditions in the marsh upstream of the mudflats were much fresher during the wet season. Both tidal channels are tributary to small watersheds, so base flow in the channels during the wet season was much greater than at the end of the dry season.

3. Observations

[11] Water surface, velocity, and salinity time series at the three stations for the dry season (Figure 2) and wet season (Figure 3) summarize the spatial and seasonal variability in the data. Although the experiments captured a range of flow conditions on the mudflats, the analysis we present here will focus on a small subset of the data, at the inner channel station during the wet season. Data from the other stations and during the dry season provide context for these results. During both dry and wet season experiments, tidal forcing was mixed semi-diurnal with amplitude of about 2 m. Inundation of the instrument frames depended on tidal stage relative to the local bed elevation. The water surface time series are relative to the tidal datum and reflect the different bed elevations (Figures 2a–2c and 3a–3c).

[12] During the dry season the maximum velocity magnitude ranged from less than 10 cm/s on the flats to about 40 cm/s in the channel (Figures 2d–2f). The water column was well mixed, and forcing was generally a balance
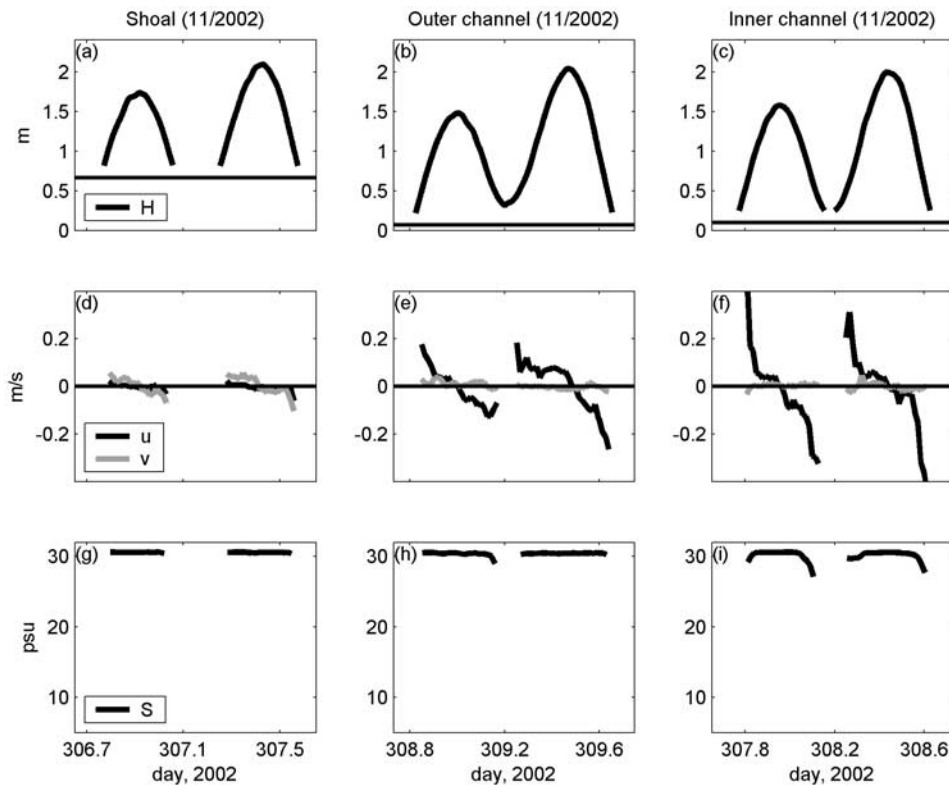
Figure 2. Water depth, velocity, and salinity on the mudflats during the dry season experiment (11/2002). The observations correspond with the stations marked in Figure 1: mudflat shoals, outer channel, and inner channel. (a–c) Water surface relative to the tidal datum (local bed elevation is the solid line). (d–f) Velocity rotated onto the primary flow axis for each station, with u along and v across the primary flow axis. The velocity measurements are 25 cm above the bed. (g–i) Salinity measured 15 cm above the bed.

between the tidal pressure gradient and bottom friction. Salinity at all three mudflat stations was approximately the same as in the bay, about 30 psu (Figures 2g–2i). At lower low water in the channel there was a slight freshening, but with little precipitation during the preceding months the freshwater input to the channel was very low and probably due to urban or industrial discharges.

[13] Conditions during the wet season were marked by much lower salinity than the dry season, with freshening both downstream in San Francisco Bay and upstream in the marsh (Figures 3g–3i). Salinity ranged from roughly 25 psu in the bay to nearly fresh in the marsh over just a few kilometers. This created very large and variable gradients in salinity, both vertically and longitudinally. While mudflat shoals were inundated for only part of the tidal cycle, the channel stations experienced a wide range of salinity and periodic stratification. To consider how salinity stratification affects flow and transport in the system, we focus on the subtidal channel during the wet season.

3.1. Velocity

[14] Because of the mixed semidiurnal tide, each 25-hour period can be divided into strong flood, weak ebb, weak flood, and strong ebb tidal phases. The strong/weak asymmetry appears in the velocity record at each station (Figures 3d–3f). Velocities have been rotated onto primary flow axes, with u in the primary flow direction and v

perpendicular to u; floods are positive u and ebbs are negative. At each location the velocity was approximately 90° out of phase with the water surface, characteristic of a standing wave. This phasing corresponds with the depth-averaged analytical model of *Fagherazzi et al.* [2003] for tidal flow in a small basin with similar geometry.

[15] Throughout the tidal cycle, velocity on the shoals was relatively low, with a maximum magnitude of about 10 cm/s (Figure 3d). The maximum velocities in the outer channel were about twice that, with greater diurnal inequality (Figure 3e). At the inner channel location, the velocity magnitudes were the largest observed, up to 40 cm/s in water depth of less than 0.5 m (Figure 3f). As the mudflats wet during the strong flood and again as they were exposed during the strong ebb, flow was shallow and bathymetrically constrained to the channel. This occurred at approximately the same time as the maximum rate of change of water surface for the rising and falling tides, and generated relatively large velocities and shears in an otherwise low energy system.

3.2. Salinity and Stratification

[16] As with velocity, there was significant salinity heterogeneity across the mudflat. On the shoals the salinity was almost always equal to conditions in the bay (Figure 3g). The outer channel remained inundated for more of the tidal cycle than the shoals, so there was fresher water when the
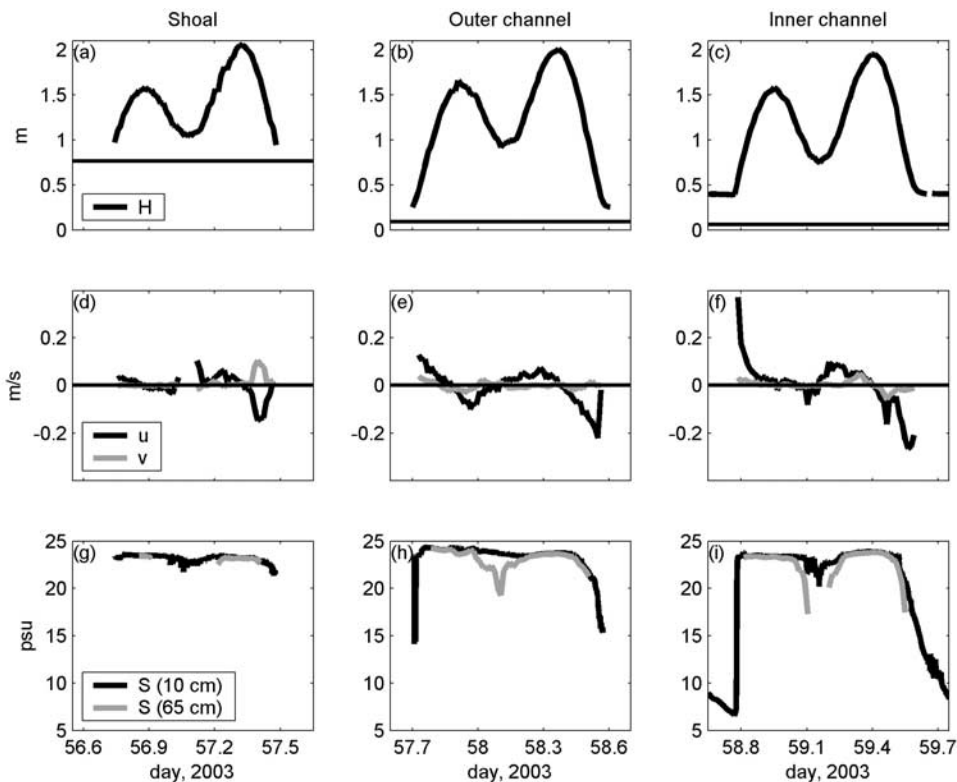
Figure 3. Water depth, velocity, and salinity on the mudflats during the wet season experiment (2/2003) at the same stations as the dry season experiment (Figure 2). (a–c) Water surface relative to the tidal datum (local bed elevation is the solid line). (d–f) Velocity measured 25 cm above the bed and rotated onto primary flow axis, with u along and v across the primary flow axis. (g–i) Salinity measured 10 and 65 cm above the bed.

sensors wet early in the flood and as they were exposed during the strong ebb (Figure 3h). Stratification developed during the weak ebb as the top sensor freshened while the bottom sensor remained at bay salinity; the water column was again homogeneous during the weak flood. The channel narrows and flow deepens moving up the channel, so the tidal variability in salinity was more apparent at the inner channel station (Figure 3i). Conditions were fresher around low water, and stratification between sensors increased during both ebbs. The magnitude of variability is worth noting, with a range of nearly 20 psu over a tidal cycle.

[17] Focusing on the subtidal channel, we consider an additional two days of data near the inner channel station. In the additional data, the variability in salinity and stratification repeats each tidal cycle (Figure 4). In a typical sequence, the strong flood brings a very rapid salinity increase as bay water moves up the channel. Salinity at the instruments then remains nearly constant through the remainder of the flood. During the weak ebb, salinity drops, particularly near the surface. Strong stratification develops and $N^2 = -g/\rho_0(\Delta\rho/\Delta z)$ becomes very large, up to $\sim 10^{-1}$ s^{-2}. The N^2 are based on measurements from instruments at three fixed elevations, and because of the close vertical placement of the sensors we cannot confidently resolve N^2 below about 1×10^{-3} s^{-2}. Although this resolution limit would be considered stratified in many settings, it is substantially less than the maximum N^2

observed during ebbs. During the weak flood, salinity increases and stratification decreases. Finally, as the marsh drains during the strong ebb, salinity steadily declines and the stratification again increases.

[18] Though the 3 days of data here are a small sample, we are confident that the pattern is not a transient response to a precipitation event but instead is generally representative of wet season conditions. A longer duration field experiment in February 2002 at this same location found similar salinity variability over 2 weeks. An anomaly in the February 2003 data is at t = 60.65 d, when the salinity decline through the ebb ceases and instead salinity remains nearly constant. This corresponds with a period of strong wind from the south. The mudflat is south facing, so wind from the south pushed bay water up the channel and halted the ebb of fresher water out of the marsh. After the wind decreased fresher water again began to flow past the instruments, and shortly thereafter the flood tide brought salinity back up to bay conditions. To remove the effects of such wind events on the mean flow and turbulence quantities ($\overline{u'u'}$, $\overline{u'w'}$, etc.) we have eliminated from the analysis times with significant wind from the south (wind speed ≥ 2.5 m/s and direction between 120° and 240°).

[19] To collapse the several days of data we use tidal phase as an indicator of conditions through much of the following analysis. Tidal phase is denoted by water depth
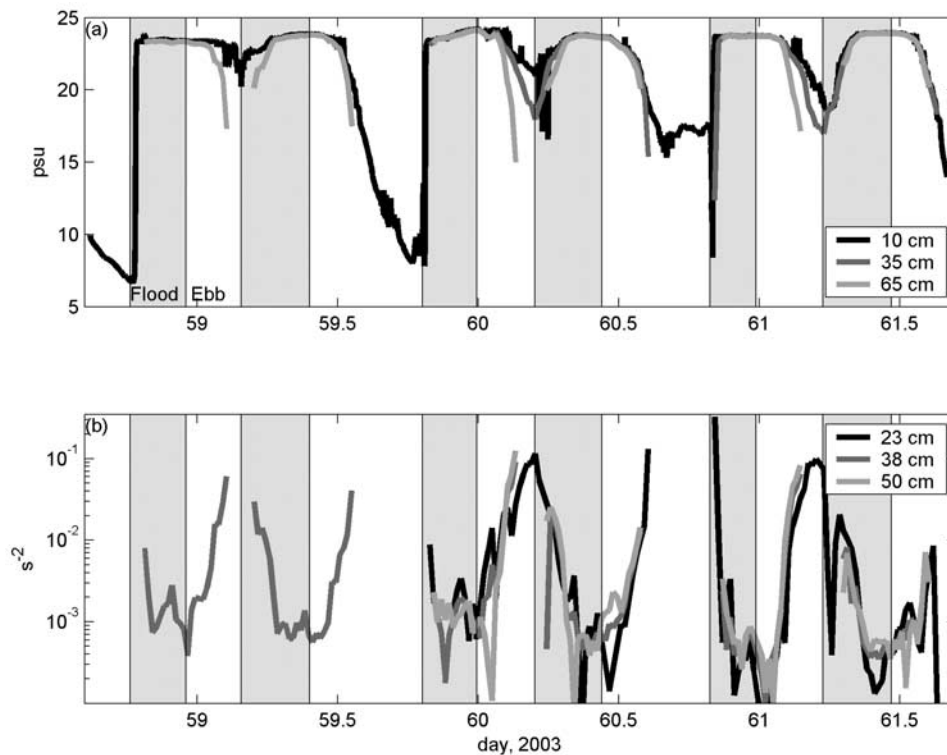
Figure 4. (a) Salinity and (b) stratification (N^2) at the inner channel station during the wet season experiment. Two salinity sensors (10 and 65 cm above the bed) were at the location for the first day (t < 59.7 d), and a third salinity sensor was added for the second and third days (t > 59.7 d). N^2 is calculated from differences between the fixed elevation salinity sensors. Flood periods are shaded.

(small at beginning of flood and end of ebb, large at high slack) and by whether the water surface is rising (flood) or falling (ebb). Velocity through the tidal cycle has been binned by water depth and divided into the four tidal phases: strong flood, weak ebb, weak flood and strong ebb (Figures 5a–5d). Generally, velocity and water depth are inversely related (large velocity at small depth, small velocity at large depth), and velocities are larger with strong tidal forcing than with weak. Stratification has an even more distinct correlation with tidal phase (Figures 5e–5h). Through most of the tidal cycle, N^2 is inversely related to depth, increasing during the falling ebbs and decreasing during the rising weak flood. An exception is at the beginning of the strong flood when N^2 is quite large. Strong stratification during the flood is not necessarily expected, but later we consider with the numerical model how this feature forms. Later in the strong flood, N^2 is relatively low and constant.

4. Turbulence and Stratification

[20] The tidally variable and asymmetric stratification are likely to affect water column turbulence differently through the tidal cycle. Stable stratification suppresses turbulent motions, while unstable stratification is a source of convective turbulence. At the same time, turbulent motions mix vertical salinity gradients and destroy stable stratification. The balance between stratification and turbulence is crucial for flow dynamics in the system. We quantify flow conditions with dimensionless numbers that compare the

relative strength of turbulence and stratification through the tidal cycle.

4.1. Bulk Richardson Number

[21] With point measurements of velocity and salinity we calculate a bulk Richardson number (Ri_b) to measure the balance between stratification and turbulence,

$$Ri_b = \frac{-g\Delta\rho\Delta z}{\rho_0(\Delta u)^2}, \qquad (1)$$

where Δu is the difference between two ADV velocity measurements, $\Delta\rho$ comes from fixed salinity and temperature measurements, and Δz is the distance between instruments. As with stratification, there is substantial variability in Ri_B through the tidal cycle (Figure 6a). During floods, Ri_b is low and fairly constant, while during ebbs it steadily increases. Though this bulk Richardson number is not necessarily tied to a critical value of 0.25 as the gradient Richardson number is, the variability in Ri_b suggests transitions between well-mixed, active turbulence during floods and stratified, suppressed turbulence during ebbs.

[22] Because of instrument configurations, $\Delta\rho$ and Δu are not centered at the same elevation during the first day at the inner channel station. Shear and stratification are not necessarily constant through the water column, so Ri_b and similar measures of stratified turbulence are less accurate during this initial day than during the following two days with additional instruments. While the tidal variability for Ri_b has a similar pattern throughout the experiment (not
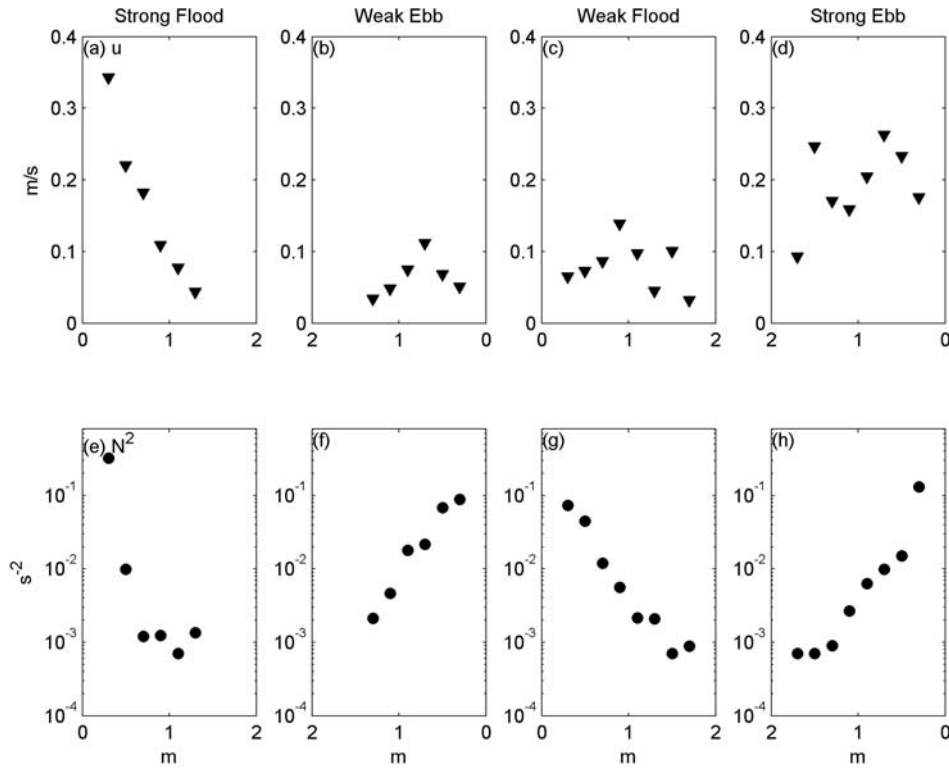
Figure 5. (a–d) Along channel velocity and (e–h) N^2 at the inner channel ~ 25 cm above the bed, bin averaged by water depth and divided into four periods by tidal forcing: strong flood, weak ebb, weak flood, and strong ebb.

shown), the magnitude of Ri_b with slightly offset $\Delta\rho$ and Δu is greater than with collocated instruments during the final two days. The offset between $\Delta\rho$ and Δu was not large (~ 15 cm), but was significant because of the strong vertical gradients. Consequently, we will concentrate the remainder of the analyses on the final two days with collocated instruments.

4.2. Length Scales

[23] For much of the turbulent length scale analyses we follow the approach detailed by *Stacey et al.* [1999]. The field experiments did not directly measure dissipation, so to calculate l_O and l_K we assume that dissipation approximately balances shear production, or $\varepsilon \sim P$. Shear production is $P = -\overline{u'w'}(\partial U/\partial z)$ where $\overline{u'w'}$ is the Reynolds stress calculated from 5-min bursts. The modified Ozmidov scale then is

$$l_O = \left(\frac{-\overline{u'w'}\,\partial U/\partial z}{N^3} \right)^{1/2} \qquad (2)$$

and the modified Kolmogorov scale is

$$l_K = \left(\frac{\nu^3}{-\overline{u'w'}\,\partial U/\partial z} \right)^{1/4}. \qquad (3)$$

To limit contamination of $\overline{u'w'}$ by low frequency, non-turbulent motions, we high-pass filter the velocity signal

before calculating $\overline{u'w'}$. The cut-off frequency for the filter was set at 0.35 s^{-1} to exclude frequencies below the largest measured N^2 but retain most turbulent timescales.

[24] For the dominant turbulent length scale we use a modified Ellison scale, but another common measure of turbulent motions is the Prandtl mixing length that has $\overline{u'w'}$ instead of $\overline{u'u'}$: $l_M = [\overline{u'w'}/(\partial U/\partial z)^2]^{1/2}$. Through most of this data set the ratio of the turbulent length scales l_E/l_M is approximately equal to the expected value of 3 [*Stacey et al.*, 1999]. Choosing l_M instead of l_E as the dominant turbulent overturn scale would shift the results by a constant factor but would not change the overall conclusions.

[25] Time series of dimensionless numbers calculated from the turbulent length scales are indicative different stages of the turbulence through the tidal cycle. Numerous investigators have found that buoyancy begins to affect turbulence around Fr_t equal to 1 [*Ivey and Imberger*, 1991; *Itsweire et al.*, 1993]. On the basis of Fr_t, conditions at this site appear to transition between active turbulence ($Fr_t > 1$) and buoyancy influence ($Fr_t < 1$) (Figure 6b). During strong floods, Fr_t is greater than 1, but as the weak ebb progresses and stratification intensifies, Fr_t drops below 1 and remains there until midway through the following weak flood. Similarly, the time series of Fr_γ varies with stratification. Values of Fr_γ less than about 3.9 are suggestive of buoyancy forcing strong enough to suppress turbulent overturns [*Ivey and Imberger*, 1991; *Luketina and Imberger*, 1989]. The pattern for Fr_γ is similar to Fr_t, with Fr_γ falling below this transition near the end of weak ebbs (Figure 6c). During this low-energy period, turbulent
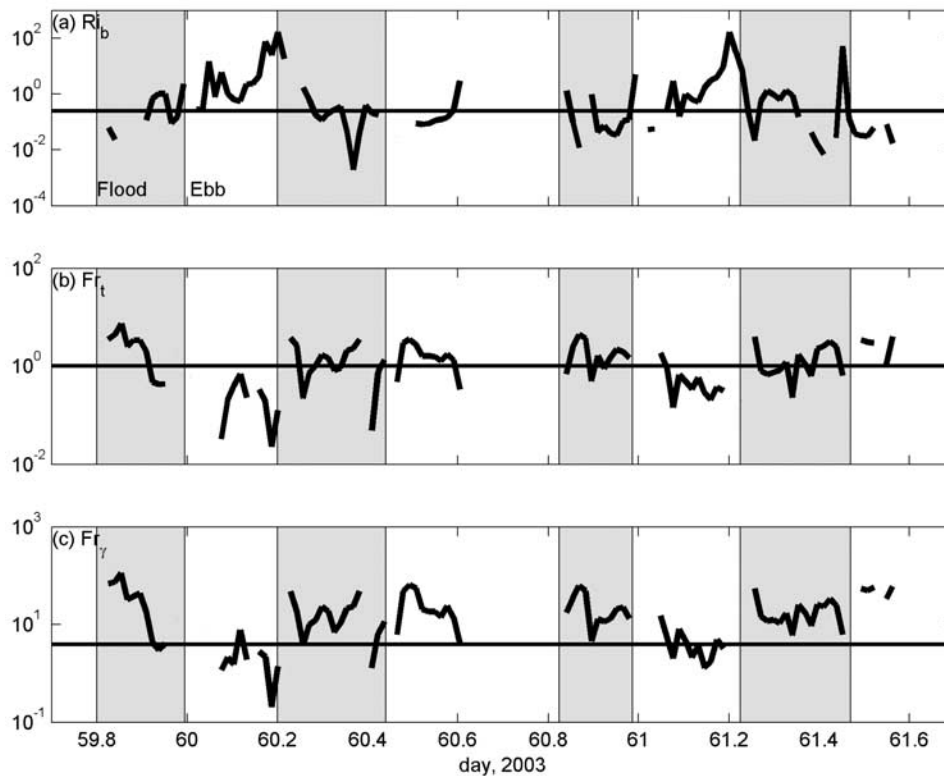
Figure 6. Dimensionless numbers at the inner channel station about 25 cm above the bed. (a) Bulk Richardson number (reference line at $Ri_b = 0.25$); (b) turbulent Froude number (reference line at $Fr_t = 1.0$); and (c) small-scale Froude number (reference line at $Fr_\gamma = 3.9$). Flood periods are shaded.

motions are severely inhibited or perhaps completely extinguished. On the basis of noise limits of the ADVs, the calculated $\overline{u'w'}$ during this period cannot be distinguished from instrument noise.

[26] To summarize flow conditions, the dimensionless numbers can be arranged as a phase diagram of Re_t against Fr_t [*Ivey and Imberger*, 1991]. Data from the subtidal channel are plotted as an $Fr_t - Re_t$ phase diagram, but separated into four tidal phases and binned by water depth (Figure 7). The $Fr_t - Re_t$ diagrams indicate very different stratification and turbulence during the different tidal phases. During the initial strong flood, data generally fall in Region I where turbulence is relatively unaffected by stratification (Figure 7a). This is true through the strong flood, with turbulence conditions independent of progression through the tide. The weak ebb is very different (Figure 7b). Around high water, there is little stratification and turbulence is relatively uninhibited. As the water level drops through the weak ebb, stratification becomes more pronounced and suppresses turbulent motions (Region II). Finally, around low water, conditions move from suppressed turbulence to collapsed turbulence because of the strong stratification (Region III). The weak flood follows, essentially reversing the weak ebb (Figure 7c). At low water, stratification is substantial and conditions are around the transition from Region II to III. Because turbulence is likely extinguished at this point, turbulent motions are not responsible for the subsequent decrease in stratification. Instead, tidal straining early in the weak flood reduces stratification until turbulent mixing can

again occur (in Region II). By the end of the weak flood, conditions have returned to isotropic turbulence of Region I. Finally, the progression through the strong ebb is similar to the weak ebb (Figure 7d). Stratification increases as the water surface falls, and turbulence is steadily more affected moving from Region I toward Region II. Because of the stronger tidal forcing, the flow is more energetic than during the weak ebb and data are shifted to larger Fr_t and Re_t at similar stages of the tide.

4.3. Turbulent Mixing

[27] Stable stratification inhibits turbulent mixing, so variable stratification through the tidal cycle has implications for the vertical mixing of salt and other scalars in the system. We start by considering the eddy viscosity, $\nu_t = -\overline{u'w'}/(\partial U/\partial z)$. The eddy viscosity can be scaled as $\nu_t \sim \alpha_t * U * H$, where α_t is a constant, U is the depth averaged velocity, and H is the water depth. Assuming unstratified flow with a parabolic distribution for υ_t, a logarithmic velocity profile, and a drag coefficient of 0.0025, an estimate for the depth-averaged eddy viscosity is $\upsilon_t \sim 3 \times 10^{-3} * U * H$ [*Fischer et al.*, 1979]. Clearly, these assumptions are not always true for the subtidal channel.

[28] Velocity and depth are correlated, so $U * H$ has a tidal signal (Figure 8a). Plotting υ_t against $u * H$ we can see how scaling for υ_t applies to this system; note that the slope of υ_t vs. $u * H$ is the scaling factor α_t. Again the data are separated by tidal phase (Figures 8b−8e). The resulting α_t are 3 to 6×10^{-4}, roughly an order of magnitude less than the
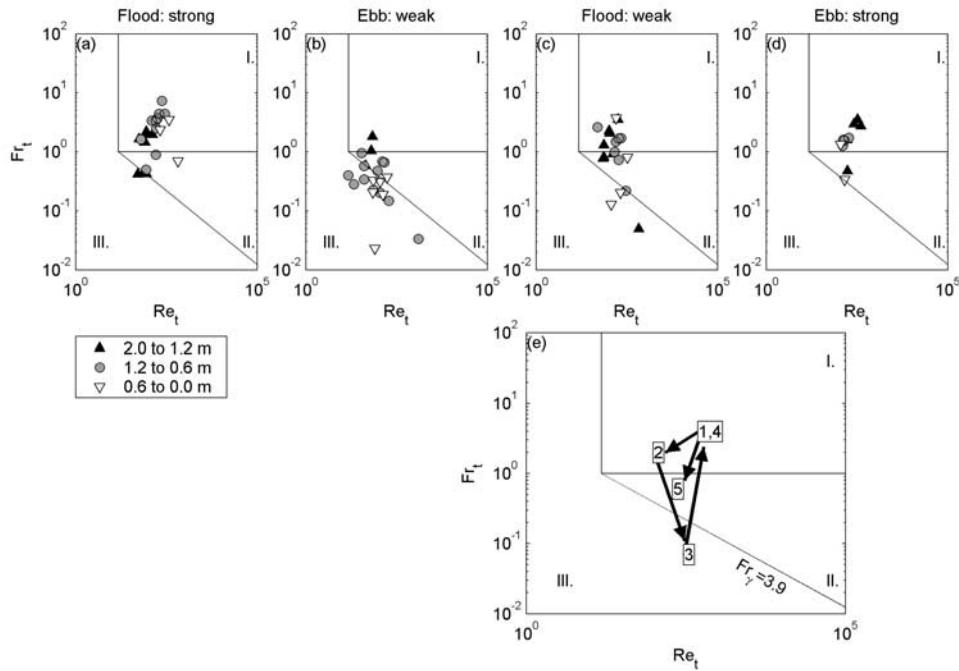
Figure 7. Re_t versus Fr_t phase diagrams for (a) strong flood, (b) weak ebb, (c) weak flood, and (d) strong ebb. Data are binned by water depth into three depth ranges. (e) Schematic summarizing the tidal cycle: (1) beginning of strong flood, (2) high slack after strong flood, (3) low slack after weak ebb, (4) high slack after weak flood, and (5) end of strong ebb. See text for description of Regions I, II, and III of phase diagram.

unstratified value. The trend for α_t between tidal phases reflects the changing stratification. Stratification inhibits mixing and consequently reduces both υ_t and α_t. In this case α_t is largest during the strong flood (5.8×10^{-4}), and drops during the stratified strong ebb (3.1×10^{-4}). Linear fits during the weak flood and ebb are not as definitive because these periods do not have large ranges of u^*H, but in general the slopes appear to be less than during the strong flood. Estimates of turbulent mixing during the weak ebb may be suspect when Fr_γ was less than 3.9 and velocity fluctuations were near instrument noise limits. All of the α_t are lower than the unstratified value of 3×10^{-3}. Instrument limitations set the lower bound for N^2 at about 1×10^{-3} s^{-2}, but conditions with N^2 less than this limit are not necessarily unstratified. Also, the choice of H as a mixing length scale may be inappropriate, particularly in strongly stratified conditions. As we discuss later, numerical model results indicate that the boundary layer during floods does not extend to the surface. In that case the height of the velocity maximum may be a more relevant mixing length scale. Regardless, the trend between tidal phases does indicate that at times the vertical transfer of momentum is affected by stratification.

[29] Using Fr_t to characterize flow conditions we can see directly how υ_t and α vary with stratification. Eddy viscosity increases with Fr_t, indicative of decreasing stratification and stronger turbulence (Figure 9a). Similarly, α_t increases with Fr_t and more active turbulence; instantaneous values of α_t are consistent with the slopes of υ_t vs. u^*H plots (Figure 9b). Results are similar comparing υ_t and α_t against Ri_b, but with opposite trends because larger

Ri_b corresponds with greater stratification. Either approach indicates that stratification is strong enough to damp turbulence and decrease the vertical momentum transfer. Damped turbulent mixing with stratification is consistent with other estuarine observations [e.g., *Peters*, 1997].

[30] In addition to momentum, we can also calculate how the vertical flux of scalars is limited by periodic stratification. Vertical mass flux is a gradient transport process like momentum: $-\overline{\rho'w'} = K_\rho(\partial\rho/\partial z)$, where K_ρ is an eddy diffusivity. The equation can be rewritten in terms of the buoyancy flux, $B = (g/\rho_0)\,\overline{\rho'w'}$. Solving for K_ρ, the result is

$$K_\rho = \frac{B}{N^2} = R_f\frac{P}{N^2}, \qquad (4)$$

where R_f is the flux Richardson number, the ratio of buoyancy to shear production: $R_f = B/P$. We can estimate R_f from the calculated Fr_t [*Ivey and Imberger*, 1991]. R_f is a measure of mixing efficiency, with a maximum of about 0.2 corresponding with $Fr_t \sim 1$. At high Fr_t, R_f tends toward zero as very energetic shear production dominates buoyancy. At low Fr_t, R_f also tends toward zero as buoyancy suppresses mixing in very low energy flow.

[31] Much like ν_t, K_ρ is variable through the tidal cycle with stratification. The eddy diffusivity increases with Fr_t as the flow becomes more energetic and less affected by stratification (Figure 9a). We scale K_ρ as $\alpha_\rho^*U^*H$ and see how the coefficient α_ρ depends on the stratification. The plot of α_ρ against Fr_t indicates that when the flow is affected by stratification ($Fr_t \leq 1$), mixing is suppressed and α_ρ is low (Figure 9b). When turbulence is relatively
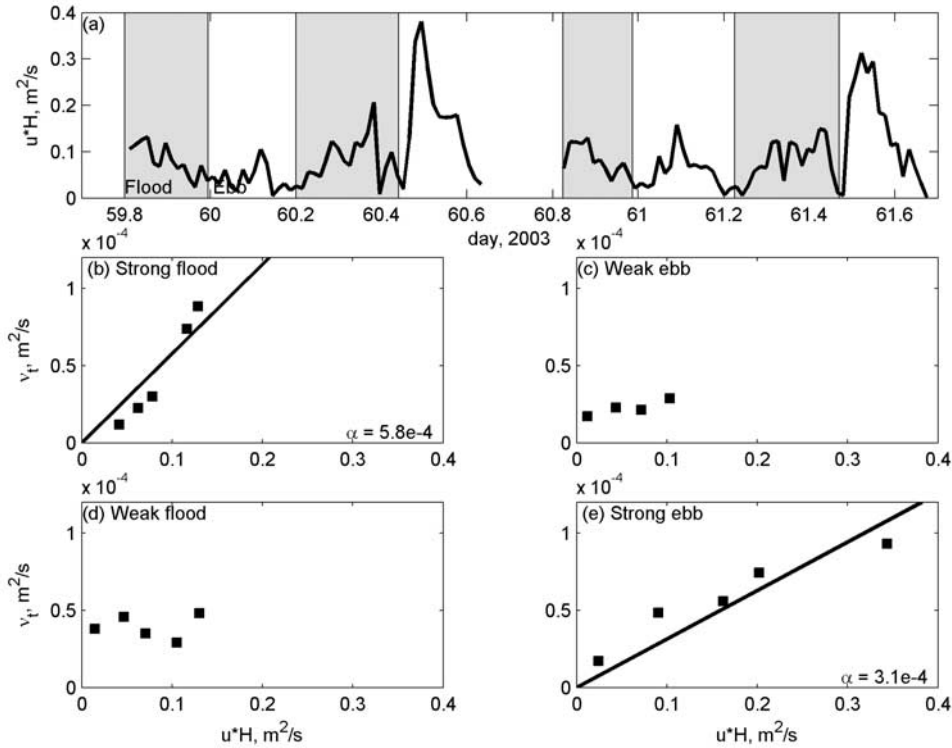
Figure 8. (a) Time series of water depth*velocity (U*H). Flood periods are shaded. Eddy viscosity (ν_t) as a function of U*H for the four tidal phases: (b) strong flood, (c) weak ebb, (d) weak flood, and (e) strong ebb. For each phase α is the slope of the best fit line of ν_t versus U*H.

unaffected by stratification (Fr$_t \geq 1$), α_ρ approaches a constant value of roughly 3×10^{-4}. This α_ρ is somewhat less than α_t at high Fr$_t$, implying a Prandtl number of about 2. The maximum α_ρ is less than would be expected in completely unstratified conditions, indicating that weak stratification may limit mixing even in during the relatively unstratified floods.

[32] The length scale and phase diagram analyses indicate that turbulence and stratification vary substantially through the tidal cycle with distinct asymmetries between ebb and flood. Stratification generally increases through ebbs and decreases through floods over a large range of N^2. Stratification suppresses turbulent motions, so the tidal asymmetry affects both flow dynamics and scalar mixing. Over time, ebb/flood asymmetries in turbulence and mixing can affect net scalar transport including the salt balance and sediment flux in the system. We now consider mechanisms behind the observed tidal asymmetries in stratification and turbulence.

5. Development of Tidal Asymmetries

[33] The analyses so far have developed around data from a single location in the channel. To understand how the tidal variability develops, we must consider the observations in the context of the entire intertidal system. Each tidal cycle, a front of salty bay water moves up across the intertidal zone and into the marsh; most of that water returns to the bay by the next lower low water. Conditions at the instrument frame change rapidly as the salinity front propagates past it and the flow dynamics there reflect

buoyancy and turbulence at the front. Despite the limited spatial coverage of the field data, we must consider the larger scale forcing that creates tidal asymmetries in stratification and mixing.

5.1. Longitudinal Salinity Gradient

[34] The asymmetries in stratification depend on the longitudinal salinity gradient $\partial S/\partial x$ through tidal straining. Unfortunately, because of instrument failure, we do not have salinity records at two points along the channel to measure $\partial S/\partial x$ directly. However, we can use the salt budget at one location to solve for the implied $\partial S/\partial x$. The salt budget is

$$\frac{\partial S}{\partial t} + U\frac{\partial S}{\partial x} + V\frac{\partial S}{\partial y} = \frac{\partial}{\partial z}\left(K_\rho \frac{\partial S}{\partial z}\right), \tag{5}$$

where U is the along-channel velocity and V is the across-channel velocity; the terms represent unsteadiness, longitudinal advection, lateral advection, and vertical mixing of salt. Because U $\gg$ V, we assume that lateral advection is small compared to longitudinal advection. We ignore vertical mixing because the timescale for advection ($\Delta x/U \sim 10^3$ s, where Δx is the width of the salinity front) is short compared with the timescale for mixing (($\Delta z)^2/K_\rho \sim 10^4$ s, where $K_\rho \sim 10^{-4}$ m^2/s from above and $\Delta z \sim 1$ m is the water depth). This scaling argument is most appropriate near the salinity front, but this is where we are most interested in the magnitude of $\partial S/\partial x$. The salt budget simplifies to a balance between unsteadiness and advection of $\partial S/\partial x$,
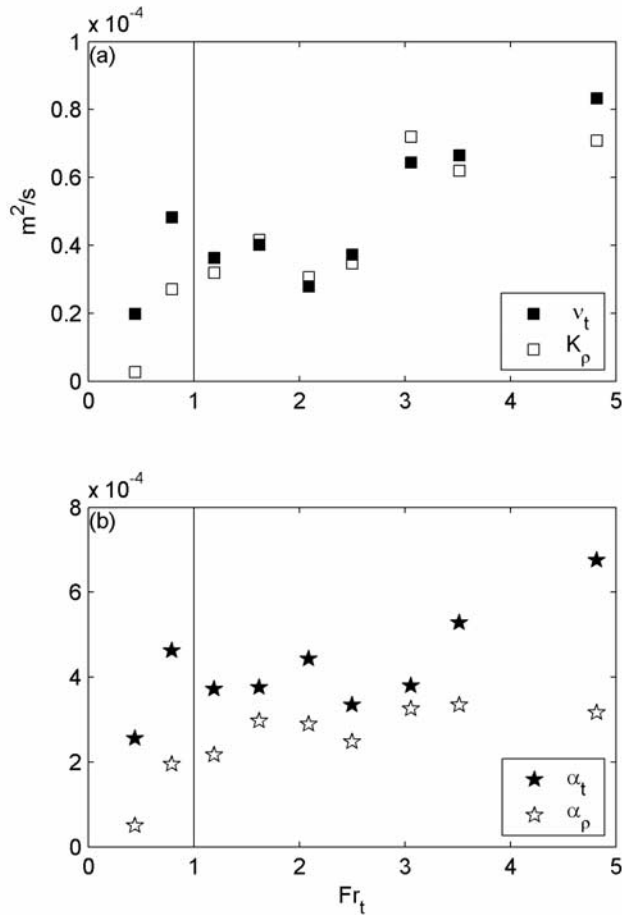
Figure 9. Mixing parameters bin averaged by Fr_t: (a) eddy viscosity ν_t and eddy diffusivity K_ρ; (b) scaling coefficients α_t and α_ρ. The results indicate stronger vertical mixing of momentum and mass with increasing Fr_t.

and salinity and velocity time series can be used to calculate $\partial S/\partial x$ (Figure 10),

$$\frac{\partial S}{\partial x} = -\frac{1}{U}\frac{\partial S}{\partial t};\qquad(6)$$

this is similar to the approach of *Geyer et al.* [2000]. Consistent values of $\partial S/\partial x$ at three elevations in the water column support the assumption that the vertical mixing term is small.

[35] The longitudinal salinity gradient at the instrument frame varies over a wide range, with maximum values each tidal cycle of about 50 psu/km. The $\partial S/\partial x$ observed here are much larger and more variable than found in most estuaries. In Central San Francisco Bay during the study period $\partial S/\partial x$ was 0.4 ± 0.2 psu/km, a factor of 100 less than the maximum values in the subtidal channel (USGS data, available at http://sfbay.wr.usgs.gov/access/Fixed_sta/). However, the large $\partial S/\partial x$ calculated from an advective/unsteady balance are supported by additional observations at the field site. Salinity measurements between two locations in the channel confirm the magnitude and timing of the salinity gradient [*Ralston and Stacey*, 2005].

[36] The large magnitude $\partial S/\partial x$ combined with shear in the along-channel velocity creates very strong buoyancy input at the front. This tidal straining provides a stabilizing flux that enhances stratification and suppresses turbulence during ebbs. During floods, straining of $\partial S/\partial x$ has the opposite effect and destratifies by adding turbulent energy. The stratification asymmetry develops through asymmetry in velocity shear, but the strong longitudinal gradients are distinctive to the intertidal system and result in exceptionally strong vertical gradients.

[37] To understand how the sharp salinity front develops each tidal cycle, we introduce a numerical model of the intertidal zone. The tidal, residual, intertidal mudflat model (TRIM) is a three-dimensional finite difference code for flow and scalar transport [*Casulli and Cattani*, 1994; *Gross et al.*, 1998]. TRIM solves the Reynolds-averaged
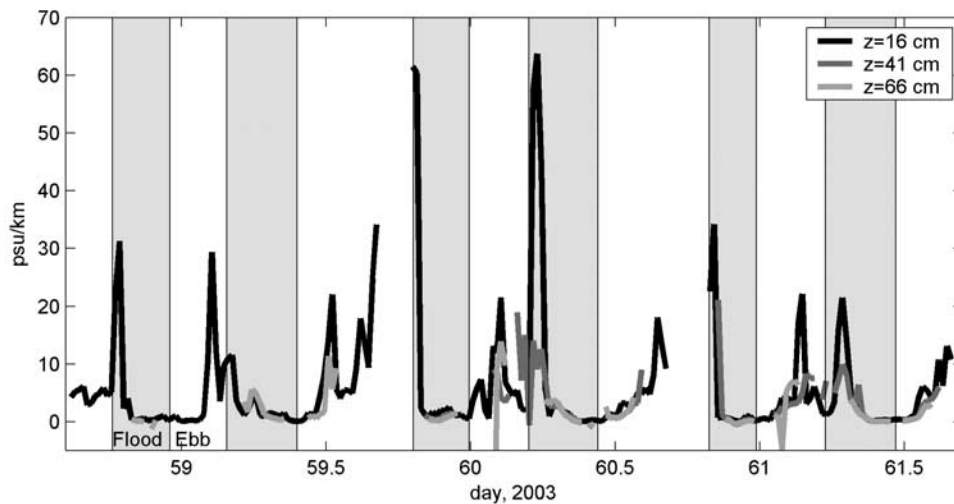

Figure 10. Longitudinal salinity gradient ($\partial S/\partial x$) calculated from an advective salt balance. The results from salinity time series at three elevations (16 cm, 41 cm, and 66 cm) are similar. Flood periods are shaded.
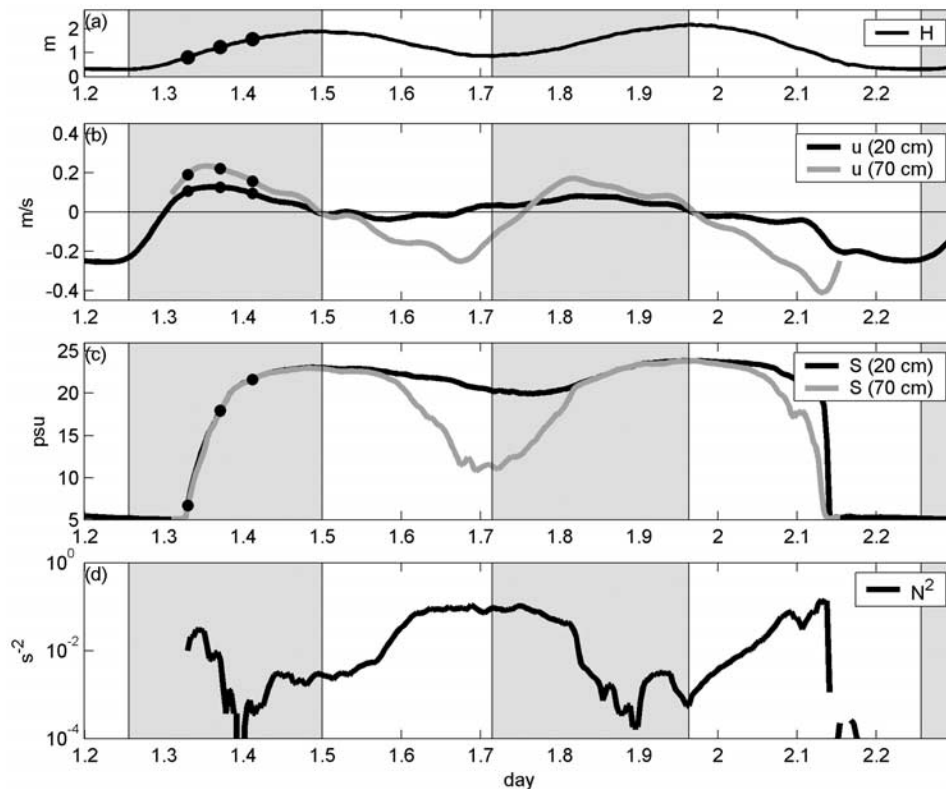
Figure 11. Numerical model results: (a) water depth, (b) along-channel velocity at 20 and 70 cm above the bed, (c) salinity at 20 and 70 cm above the bed, and (d) and N^2 averaged between 20 and 70 cm above the bed. The data are sampled from the subtidal channel to correspond with the location of the inner channel station of field observations. Circles marked on the time series indicate the times of the along-channel profiles in Figures 12 and 13. Flood periods are shaded.

Navier-Stokes equations, parameterizing turbulence with Mellor-Yamada Level 2.5 closure [*Galperin et al.*, 1988]. An important feature for this intertidal application is that the model efficiently handles wetting and drying of cells. TRIM has been successfully applied to several estuarine settings, including South San Francisco Bay [*Cheng et al.*, 1993; *Gross et al.*, 1999].

[38] The grid for the model is a vastly simplified version of the field site: a straight subtidal channel with intertidal flats on either side. The domain has a constant slope of 0.0005, a value consistent with the bathymetry at the field site. The grid spacing is 10 m horizontally and 0.1 m vertically. At the closed upstream end of the domain is a reservoir of relatively fresh water (5 psu), and at the downstream end is an open boundary at bay salinity (25 psu). To compare numerical results with the observations, the open boundary condition was forced with a NOAA station record of water surface elevation during the deployment, but a simple sinusoidal water surface boundary condition gives similar results. The model requires only a very brief spin-up to reach a periodic steady state because with each lower low water the domain drains and conditions essentially reset. The numerical results are similar during each 25-hour tidal cycle, so we present just one such period.

[39] The model bathymetry does not reflect the complexity of the field site (or most natural systems), so we do not expect the numerical results to exactly replicate the field data. However, even with this very simple geometry the model does reproduce important features of the observations quite well. Sampling in the channel at a location that corresponds with the instrument frames, we extract time series for water surface, velocity, salinity, and stratification (Figure 11). For comparison with observations (Figure 3) the time series are from fixed elevations 0.2 m and 0.7 m above the bed. The water surface and velocity reflect the tidal asymmetry in the boundary condition (Figures 11a–11b). Salinity at the sample location varies between 5 and 25 psu over a tidal period, with a sharp increase during the initial flood and a steadier decline during the strong ebb (Figure 11c). The pattern and magnitude of the stratification is also similar to observations, with increasing N^2 during ebbs and decreasing N^2 during floods (Figure 11d). Salinity and velocity time series compare favorably with the data, although with additional model calibration the fit could be improved. However, there is limited value in extensive tuning to such a short data record. With little calibration the simple bathymetry reproduces the major features of the observations, and conclusions drawn from the model generalize to other intertidal settings rather than solely applying to the field site.

[40] The longitudinal salinity gradient follows the same pattern as in the observations: spatially variable with very strong gradients around a tidal salinity front. The peaks in stratification correspond with large $\partial S/\partial x$ at the front. Straining of $\partial S/\partial x$ during ebbs increases stratification, and that reduces turbulent mixing and permits even greater
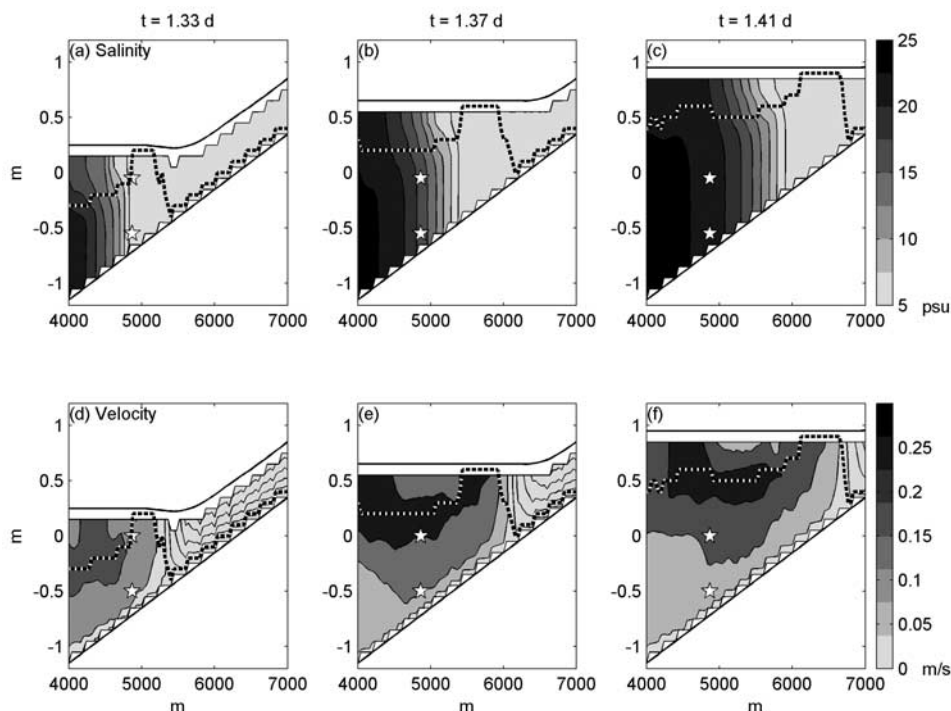
Figure 12. Numerical model results: along-channel profiles of (a–c) salinity and (d–f) velocity at three times during the strong flood. The dashed line indicates the elevation of maximum along-channel flood velocity. Stars correspond with the locations of time series plotted in Figure 11.

shear of the velocity profile. The maximum shear through both ebbs is substantially greater than the maximum shear through floods, even though the velocity magnitudes are similar (Figure 11b). As water level falls through the strong ebb, N^2 drops when the fresh edge of the front advects past the sample location (t ~ 2.15 d). The decrease in stratification toward the end of the strong ebb does not appear in the field data because the upper salinity and velocity sensors were not submerged at this depth.

[41] The salinity front is generated around each lower low water. During the strong flood the transition between fresh and salty water is a narrow zone (or brief in time at a station) and $\partial S/\partial x$ is large. As the front advects upstream, dispersion mixes the front such that when it passes the station again during the weak ebb $\partial S/\partial x$ has decreased. The weak flood pushes the frontal region back upstream and salinity returns to low gradient bay water. Finally, during the strong ebb the front is expelled from the mudflat and as it passes the sampling station $\partial S/\partial x$ increases but does not reach the initial flood maximum. Mudflats and marsh drain after a full tidal cycle, so the system completely resets and a sharp front returns with the following flood. The intertidal elevation proves fundamental to developing very strong longitudinal gradients that in turn create asymmetries in stratification and turbulence.

5.2. Vertical Structure

[42] In addition to spatial structure across the intertidal elevation gradient, the model also allows consideration of how vertical structure of the flow contributes to tidal asymmetries. As discussed previously, the water column is highly stratified and highly sheared through most ebbs.

During flood tides the vertical structure is very different: There is much less vertical shear in along-channel velocity and salinity is fairly well mixed. Stratification is weak during most floods except for the beginning of each rising tide. At the beginning of the weak flood (t ~ 1.75 d), the water column remains stratified from the previous weak ebb. As the stratified region advects back upstream, stratification mixes away and N^2 decreases (t ~ 1.85 d); N^2 remains low until the strong ebb. This decrease in stratification through floods corresponds with tidal straining of $\partial S/\partial x$ and a destabilizing buoyancy flux.

[43] During the strong flood, there is significant stratification just after the salinity front moves upstream (t ~ 1.35 d). Brief but strong stratification during the strong flood also appears in the field data as the front moves past the instruments (Figure 5b; t ~ 59.82 and 60.85 d). With resetting of conditions at lower low water we might expect the bay water advancing up the mudflats to be relatively unstratified. The model results suggest that the observed stratification depends on vertical structure of along-channel velocity.

[44] Along-channel profiles of salinity and velocity during the strong flood are marked with the sample locations of the time series (Figure 12); times of the longitudinal profiles are indicated on the time series (Figure 11). The longitudinal profiles are overlaid with the elevation of the maximum flood velocity as a dashed line. At the leading edge of the front the velocity maximum is at or near the surface, but just behind the front the velocity maximum is well below the surface (Figure 12). Above the velocity maximum, advection of $\partial S/\partial x$ provides a stabilizing buoyancy flux during floods: salty water at the velocity maximum advects upstream faster
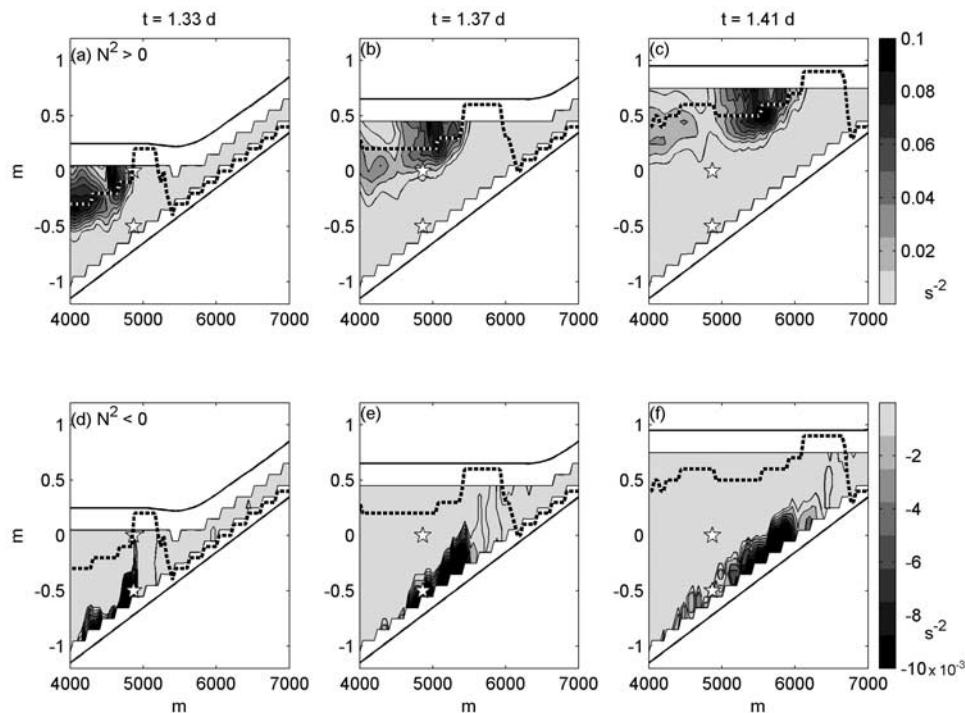
Figure 13. Numerical model results: along-channel profiles of N^2 at the same times as in Figure 12. (a–c) Stable stratification ($N^2 > 0$), (d–f) unstable stratification ($N^2 < 0$). The dashed line indicates the elevation of maximum along-channel flood velocity. Stars correspond with the locations of time series plotted in Figure 11.

than fresher water above it. This creates a large positive N^2 above the velocity maximum (Figures 13a–13c). Below the velocity maximum the longitudinal buoyancy flux is destabilizing, resulting in negative N^2 near the bed (Figures 13d–13f). Unstable stratification makes buoyancy a source of turbulent energy, although the turbulence closure does incorporate convective mixing. The field observations did not record instances of unstable stratification, but this was probably due to the limited spatial and temporal resolution of the sampling.

[45] The vertical structure of an energetic, unstratified flood boundary layer capped by stable stratification has been observed in other estuarine settings [e.g., *Stacey and Ralston*, 2005], but might not be expected in shallow mudflat flows. In this case, density-driven lateral circulation between channel and shoals helps create the subsurface velocity maximum. Dense water moves out of the channel onto shoals near the bed, and return flow at the surface brings low momentum shoal water into the channel to create a velocity deficit. The details of this lateral circulation will be considered elsewhere [*Ralston and Stacey*, 2005]. The subsurface velocity maximum and capped boundary layer during floods is consistent with mixing calculations from the field data. The scaling coefficient during floods was less than the standard unstratified value, but that could be because the appropriate mixing length scale in this case is the boundary layer height rather than the full water depth.

6. Discussion and Conclusions

[46] Tidal asymmetries in stratification and mixing in the subtidal channel appear linked to the different vertical and longitudinal flow structures during floods and ebbs. To understand the field observations at a point, we have to consider how they fit into the larger context of the intertidal system. In many ways this small, shallow system resembles much larger estuaries, but the subtidal channel is notable because it exhibits significantly stronger vertical and longitudinal salinity gradients than are found in larger systems. Because of the intertidal elevation, the mudflat/marsh system resets with each lower low water, in this case every 25 hours. Consequently, the diurnal timescale is appropriate for a conceptual model for the system. Although the field experiment did not span a spring-neap cycle, we can speculate how conditions would change with the spring tides in San Francisco Bay. Spring tides have more symmetric semi-diurnal forcing than neaps, so the strong/weak tide distinction is less important. The symmetric spring tidal amplitudes generally fall between the strong and weak forcing of neap tides, so we expect conditions during springs (or in estuaries without diurnal inequalities) to fall between the bounding cases of neap strong and weak tides.

[47] Focusing on the four tidal phases of one diurnal period, Figure 14 combines longitudinal structure with the local stratification and mixing into a conceptual summary of conditions across the intertidal elevation gradient. At the beginning of the strong flood, the salinity front is a compact region between fresher water flowing out of the marsh and saltier bay water. The salinity front moves upstream with nearly vertical isohalines except for moderate stratification immediately behind the front and above the velocity maximum (Figure 14a). During the weak ebb, isohalines are strained such that they are nearly horizontal, increasing stratification until the salinity structure is similar to a salt
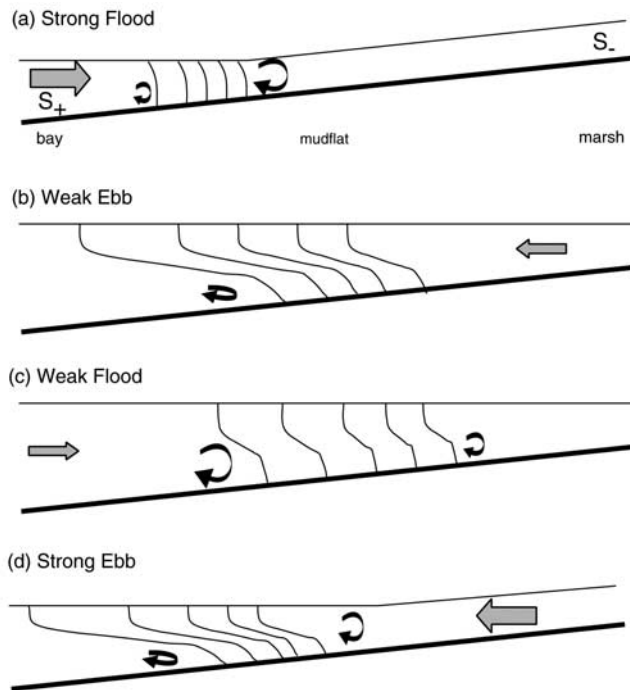
Figure 14. Schematic of periodic stratification in mudflat channel through a tidal cycle. Along-channel profiles of isohalines during (a) strong flood, (b) weak ebb, (c) weak flood, and (d) strong ebb. Horizontal arrows represent relative velocity magnitude, while circular arrows indicate relative strength and isotropy of turbulent mixing.

wedge estuary (Figure 14b). The weak flood reduces stratification so that by the end of the tide isohalines are again largely vertical (Figure 14c). Finally the strong ebb reverses the sign of the velocity shear and the front region becomes more stratified, recreating a highly stratified zone that advects out to the bay (Figure 14d). At the end of the strong ebb the intertidal region is exposed, and the system is reset. Dispersion through the tide reduces the salinity gradient, but because of the initial strength of the front and the short time between low waters the longitudinal gradient and associated buoyancy forcing remain substantial. Because of the strong longitudinal buoyancy forcing, the subtidal channel evolves through the spectrum of conditions in a partially mixed estuary in just one tidal cycle.

[48] The diagrams represent conditions in the subtidal channel, and do not necessarily coincide with conditions on the shoals. Higher elevation shoals are inundated for only part of the tide, so the phasing of their inundation with the passage of the salinity front is crucial for conditions at a given location. Exchange between channel and shoal can be important for the momentum and scalar budgets of each, but the dominant forcing is along the elevation gradient from bay to marsh. We limit the discussion here to the dynamics and tidal asymmetries along the channel axis and consider the role of channel/shoal bathymetry elsewhere [*Ralston and Stacey*, 2005].

[49] The variable stratification in the channel results in different flow dynamics between flood and ebb. During ebbs, stratification increases through the tide and Fr_t decreases. Stratification can strengthen to the point that

turbulence becomes anisotropic and mixing is suppressed. During floods, the important feature seems to be the structure of the boundary layer. Relatively unstratified active mixing occurs below the velocity maximum, while stable stratification exists above the velocity maximum. During both ebbs and floods the stratification occurs over a narrow frontal zone between two relatively well-mixed regions upstream and downstream. Different turbulence conditions during ebb and flood because of the asymmetric longitudinal forcing impact the vertical mixing of momentum and scalars in the water column, and consequently net transport across the intertidal zone.

References

Blanchard, G. F., J.-M. Guarini, F. Orvain, and P.-G. Sauriau (2001), Dynamic behavior of benthic microalgal biomass in intertidal mudflats, *J. Exper. Mar. Biol. Ecol.*, *264*, 85–100.

Casulli, V., and E. Cattani (1994), Stability, accuracy and efficiency of a semi-implicit method for three-dimensional shallow water flow, *Comput. Math. Appl.*, *27*, 99–112.

Chant, R. J., and A. W. Stoner (2001), Particle trapping in a stratified flood-dominated estuary, *J. Mar. Res.*, *59*, 29–51.

Cheng, R. T., V. Casulli, and J. W. Gartner (1993), Tidal, residual, intertidal mudflat (TRIM) model and its applications to San Francisco Bay, California, *Estuarine Coastal Shelf Sci.*, *36*, 235–280.

Christiansen, T., P. L. Wiberg, and T. G. Milligan (2000), Flow and sediment transport on a tidal salt marsh surface, *Estuarine Coastal Shelf Sci.*, *50*, 315–331.

Christie, M. C., K. R. Dyer, and P. Turner (1999), Sediment flux measurements from a macro tidal mudflat, *Estuarine Coastal Shelf Sci.*, *49*, 667–688.

Dyer, K. R., M. C. Christie, N. Feates, M. J. Fennessy, M. Pejrup, and W. van der Lee (2000), An investigation into processes influencing the morphodynamics of an intertidal mudflat, the Dollard Estuary, The Netherlands: I. Hydrodynamics and suspended sediment, *Estuarine Coastal Shelf Sci.*, *50*, 607–625.

Fagherazzi, S., and D. J. Furbish (2001), On the shape and widening of salt marsh creeks, *J. Geophys. Res.*, *106*, 991–1003.

Fagherazzi, S., P. L. Wiberg, and A. D. Howard (2003), Tidal flow field in a small basin, *J. Geophys. Res.*, *108*(C3), 3071, doi:10.1029/2002JC001340.

Fischer, H. B., E. J. List, R. C. Y. Koh, J. Imberger, and N. H. Brooks (1979), *Mixing in Inland and Coastal Waters*, Elsevier, New York.

Friedrichs, C. T. (1995), Stability shear stress and equilibrium cross-sectional geometry of sheltered tidal channels, *J. Coastal Res.*, *11*, 1062–1074.

Galperin, B., L. H. Kantha, S. Hassid, and A. Rosati (1988), A quasi-equilibrium turbulent energy model for geophysical flows, *J. Atmos. Sci.*, *45*, 55–62.

Geyer, W. R., J. H. Trowbridge, and M. M. Bowen (2000), The dynamics of a partially mixed estuary, *J. Phys. Oceanogr.*, *30*, 2035–2048.

Gibson, C. H. (1986), Internal waves, fossil turbulence, and composite ocean microstructure spectra, *J. Fluid Mech.*, *168*, 89–117.

Gross, E. S., V. Casulli, L. Bonaventura, and J. R. Koseff (1998), A semi-implicit method for vertical transport in multidimensional models, *Int. J. Numer. Methods Fluids*, *28*, 157–186.

Gross, E. S., J. R. Koseff, and S. G. Monismith (1999), Three-dimensional salinity simulations of South San Francisco Bay, *J. Hydraul. Eng.*, *125*, 1199–1209.

Itsweire, E. C., J. R. Koseff, D. A. Briggs, and J. H. Ferziger (1993), Turbulence in stratified shear flows: Implications for interpreting shear-induced mixing in the ocean, *J. Phys. Oceanogr.*, *23*, 1508–1522.

Ivey, G. N., and J. Imberger (1991), On the nature of turbulence in a stratified fluid: Part I. The energetics of mixing, *J. Phys. Oceanogr.*, *21*, 650–658.

Leonard, L. A., A. C. Hine, M. E. Luther, R. P. Stumpf, and E. E. Wright (1995), Sediment transport processes in a west-central Florida open marine marsh tidal creek: The role of tides and extra-tropical storms, *Estuarine Coastal Shelf Sci.*, *41*, 225–248.

Leopold, L. B., J. N. Collins, and L. M. Collins (1993), Hydrology of some tidal channels in estuarine marshland near San Francisco, *Catena*, 20, 469–493.

Luketina, D. A., and J. Imberger (1989), Turbulence and entrainment in a buoyant surface plume, *J. Geophys. Res.*, 94, 12,619–12,636.

Nepf, H. M., and W. R. Geyer (1996), Intratidal variations in stratification and mixing in the Hudson estuary, *J. Geophys. Res.*, 101, 12,079–12,086.

Peters, H. (1997), Observations of stratified turbulent mixing in an estuary: Neap-to-spring variations during high river flow, *Estuarine Coastal Shelf Sci.*, 45, 69–88.

Ralston, D. K., and M. T. Stacey (2005), Longitudinal dispersion and lateral circulation in the intertidal zone, *J. Geophys. Res.*, 110, C07015, doi:10.1029/2005JC002888.

Rippeth, T. P., N. R. Fisher, and J. R. Simpson (2001), The cycle of turbulent dissipation in the presence of tidal straining, *J. Phys. Oceanogr.*, 31, 2458–2471.

Shi, Z., and J. Y. Chen (1996), Morphodynamics and sediment dynamics on intertidal mudflats in China (1961–1994), *Cont. Shelf Res.*, 16, 1909–1926.

Simpson, J. H., J. Brown, J. Matthews, and G. Allen (1990), Tidal straining, density currents, and stirring in the control of estuarine stratification, *Estuaries*, 13, 125–132.

Stacey, M. T., and D. K. Ralston (2005), The scaling and structure of the estuarine bottom boundary layer, *J. Phys. Oceanogr.*, 35, 55–71.

Stacey, M. T., S. G. Monismith, and J. R. Burau (1999), Observations of turbulence in a partially stratified estuary, *J. Phys. Oceanogr.*, 29, 1950–1970.

Stevens, C. L. (2003), Turbulence in an estuarine embayment: observations from Beatrix Bay, New Zealand, *J. Geophys. Res.*, 108(C2), 3030, doi:10.1029/2001JC001221.

Wells, J. T., C. E. Adams, Y. A. Park, and E. W. Frankenberger (1990), Morphology, sedimentology and tidal channel processes on a high-tide-range mudflat, west coast of South Korea, *Mar. Geol.*, 95, 111–130.

Widdows, J., and M. Brinsley (2002), Impact of biotic and abiotic processes on sediment dynamics and the consequences to the structure and functioning of the intertidal zone, *J. Sea Res.*, 48, 143–156.

———————————

D. K. Ralston and M. T. Stacey, Department of Civil and Environmental Engineering, MC 1710, University of California, Berkeley, CA 94720-1710, USA. (dralston@berkeley.edu)